Applied Physics A (2026) 132:114
https://doi.org/10.1007/s00339-025-09288-y

Applied Physics A
Materials Science & Processing

Multi-Physics finite element modeling of PEEK in selective laser sintering: effects of laser power and scanning speed on thermal distribution and melt pool formations

Oğulcan Eren[1]

Received: 1 November 2025 / Accepted: 31 December 2025
© The Author(s) 2026

Abstract
Selective Laser Sintering (SLS) of poly(ether ether ketone) (PEEK), a high-performance polymer, presents significant challenges due to its narrow processing window, high melting temperature, and low thermal conductivity in powder form. The successful fabrication of highly functional, dense components necessitates precise control over the intricate thermal and fluid dynamics governing the PEEK sintering process. However, experimental and single-physics modeling approaches are often insufficient to capture these transient multi-physics phenomena. This study introduces a novel two-dimensional (2D) multi-physics Finite Element Analysis (FEA) model to simulate the SLS processing of PEEK powder. This study realistically models the transient thermal and fluid behaviour during the SLS process and evaluates the effect of fundamental parameters such as laser power and scanning speed by incorporating combined multi-physical phenomena such as heat transfer, fluid dynamics, and phase transformations. Although optimum thermal profiles are obtained at an Energy Density (ED) of 0.03 J/mm², it has been determined that ED is not the single factor in understanding the thermal behavior. The results show that scan speed significantly regulates heat accumulation and thermal gradients. Slower scanning speeds promote high heat buildup and surface degradation at low powers, while higher speeds limit thermal penetration, increasing the temperature difference between the top and bottom surfaces. This computationally efficient 2D multi-physics approach improves understanding of PEEK laser sintering mechanisms, providing quantitative information for rapid and effective parameter identification in high-performance polymer additive manufacturing.

Keywords Multi-physics modeling · Selective laser sintering · PEEK · Laser powder bed fusion of polymers (LPBF-P) · Finite element analysis

1 Introduction

Selective Laser Sintering (SLS), also known as Laser Powder Bed Fusion of Polymers (LPBF-P), is an additive manufacturing technique that employs a high-intensity laser to selectively fuse polymer powder layer by layer to produce solid parts. This method facilitates the fabrication of intricate polymer components without moulds or tools, utilised for manufacturing high-performance parts across various sectors, including aerospace and biomedical [1, 2]. In SLS, numerous process parameters, such as laser power, scanning speed, hatch spacing, layer thickness, and powder bed temperature, significantly influence sintering behavior and final part properties. These parameters influence melt pool formation, interlayer bonding, part density, mechanical strength, and accuracy by controlling the energy input and thermal history during layer fusion [3, 4]. For example, a higher laser power or a lower scanning speed increases the energy delivered to the powder bed, raising the peak temperature and generally resulting in less porous local fusion. However, excessive energy can also lead to overheating or degradation. Therefore, it is essential to optimize SLS process parameters to produce parts with improved quality by preventing defects. Recent studies have increasingly focused on optimizing SLS process parameters for the fabrication

✉ Oğulcan Eren
ogulcaneren@gazi.edu.tr

[1] Department of Industrial Design Engineering, Gazi University, Ankara 06500, Turkey

Published online: 21 January 2026

of high-performance polymers. Wang et al. studied the effects of interlayer temperature gradients on the flexural and tensile performance of PEEK by optimizing the laser energy density depending on the temperature field distribution [5]. Rahman et al. optimized TPU-based SLS parameters using response surface methodology, linking layer thickness and laser power ratio to density and modulus [6]. Franco et al. analyzed the SLS process from an experimental energy perspective and determined the optimum volumetric energy density for PA12 [7]. In addition to experimental processes, machine learning-focused approaches are employed for process parameter optimization and defect minimization [8]. Similarly, Borah and Chandrasekaran discussed thermal-mechanical modeling and optimization strategies for 3D printing, highlighting the shift toward data-driven and simulation-assisted frameworks [9]. On the other hand, Schmid et al. showed that PA12 powders from different origins require distinct SLS processing conditions due to differences in particle morphology, thermal behavior, and crystalline structure [10]. Here, it is important to acknowledge that the properties of the materials used are another critical factor in the optimization process.

Among high-performance SLS thermoplastics, poly(ether ether ketone) (PEEK) is distinguished by its exceptional strength-to-weight ratio, increased melting temperature (≈ 343 °C), thermal stability, and chemical inertness [11]. Nonetheless, substantial obstacles exist in effectively processing using SLS [12]. For example, to prevent the rapid cooling of recently sintered layers, the powder bed must be heated to a high preheat temperature (approximately the melting point of the polymer) during SLS processing of PEEK. If the powder bed temperature drops below the crystallization point during processing, the material may suddenly crystallize and shrink, causing layer failure or warping. PEEK also exhibits a higher melting temperature compared to more common polymers, such as polyamides, and exhibits a limited processing window between the initiation of crystallisation and melting [13]. Furthermore, PEEK has a high melt viscosity, which can prevent densification during laser sintering and restrict polymer flow [14]. These factors make parameter optimization of SLS for PEEK particularly critical. Schmidt et al. were pioneers in demonstrating the feasibility of SLS processing for PEEK, emphasising the necessity for substantial system modifications, including elevated preheating (> 300 °C) and enhanced powder flowability, in order to achieve sufficient part density [15]. Subsequent work by Berretta et al. expanded on this by introducing High Temperature Laser Sintering (HT-LS) systems capable of processing PEEK powders above 250 °C, showing that optimized energy densities between 0.018 and 0.032 J/mm² result in strong mechanical performance and reduced porosity [16]. More recent research has focused on lowering the processing temperature. Kigure et al. introduced a modified low-temperature sintering technique utilising a powder bed temperature of 170–200 °C, resulting in over 95% relative density and around 80 MPa tensile strength, demonstrating the feasibility of processing PEEK on conventional SLS machines [17]. Although these experimental studies contribute to understanding the effect of SLS parameters on the mechanical and dimensional properties of the final part, they are incapable of capturing transient phenomena like molten pool dynamics and temperature gradients during sintering.

Finite Element Analysis (FEA) provides a fundamental approach to understanding the transient, multi-physical behaviour in SLS, particularly for PEEK where thermal gradients and crystallisation play a critical role. Mokrane et al. and Riedlbauer et al. utilised FEA to simulate temperature distributions and cooling rates in polymer SLS, resulting in an excellent correlation with experimental melt pool geometries [18, 19]. Shen et al. enhanced this by incorporating viscoelastic–viscoplastic constitutive behaviour and crystallisation kinetics to forecast the evolution of residual stress in PA12 [20]. Zhang et al. compared eight volumetric heat source models and presented a new formulation that accounts for variable thermal conductivity and absorptivity, improving the prediction accuracy of melt pool dimensions [21]. Eren et al. developed a fully coupled 3D multi-physics finite element model for PA12 that incorporated transient heat transfer, melt pool evolution, phase change, and temperature-dependent viscosity to predict sintering quality under varying laser parameters [22]. However, the computational expense of such detailed 3D models limits their applicability for broad parametric studies or rapid process exploration. In the context of PEEK, few numerical models have been reported. Wang et al. recently employed FEA to simulate interface temperature distributions and optimize laser energy density, but their work did not fully couple heat transfer with viscoplastic deformation or phase change [5]. Therefore, a need remains for a multi-physics FEA framework that can simultaneously capture the laser–material interaction, melt pool dynamics, and interlayer fusion in high-temperature semi-crystalline polymers.

This study presents a computationally efficient two-dimensional multiphysics finite element model to simulate the SLS process of PEEK. It investigates the effects of laser parameters (laser power and scanning speed) on melt pool formation and temperature gradients using a multiphysics-based FEA method. This research differs

from previous studies that focused solely on experimental optimization [7, 15, 16] or single-physics simulations [5, 20] by integrating multiple physical phenomena, including heat transfer, fluid flow dynamics, melting-solidification kinetics, and phase transformations, to accurately represent the transient thermal and fluid behaviours of the SLS process. The model simultaneously assesses thermal gradients, melt pool dimensions, and interface temperature evolution, thereby offering quantitative insights into the optimal processing window that balances interlayer bonding and dimensional stability. The originality of this research lies in extending the polymer SLS modeling to the high-temperature regime of PEEK, integrating validated heat transfer and phase transition submodels, and correlating the simulation results with experimentally reported processability trends [16, 17, 23]. This enhances comprehension of PEEK laser sintering mechanisms, facilitating swift and effective identification of process parameters in high-performance polymer additive manufacturing.

2 Finite element modeling approach for selective laser sintering

2.1 Physical configuration and modeling assumptions

The SLS process is a thermophysical additive manufacturing method based on the irradiation and melting of a thin layer of polymer powder by a high-power CO_2 laser. Figure 1 schematically shows these thermal interactions. When the laser beam hits the powder bed, part of its energy is reflected, depending on the material properties, powder particle size and phase. The remaining energy is transferred to the powder and converted into heat. The attenuation of this absorbed energy into the powder bed is determined by the Beer-Lambert Law (Eq. 1). This principle, which is critical for modeling heat distribution, estimates the laser intensity I (W/mm^2) at a depth z (m) under the surface:

$$I(z) = I_0 \, e^{(\beta \cdot z)} \tag{1}$$

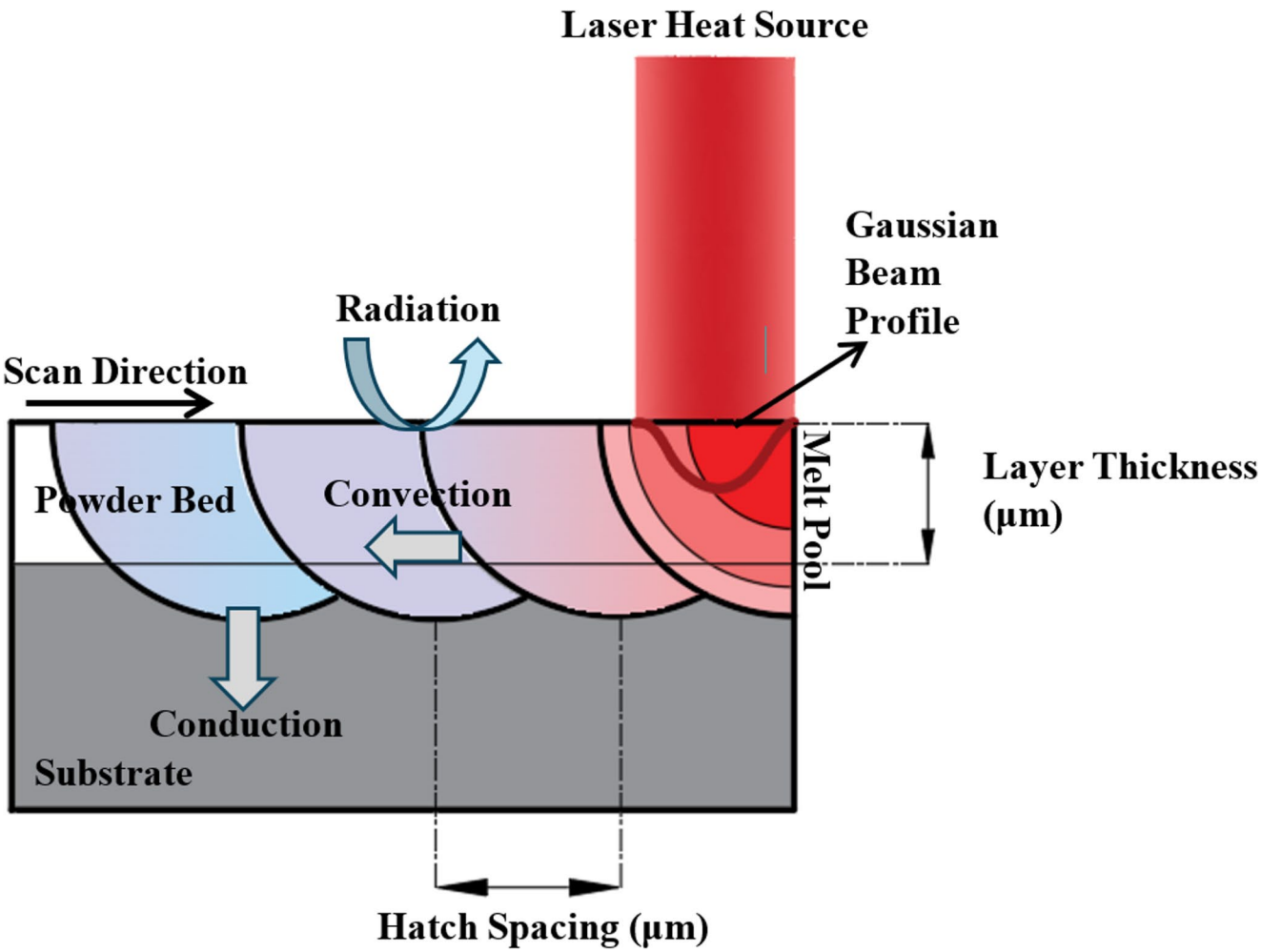


Fig. 1 Schematic of multi-physic interaction in laser-based powder bed fusion process

where β (m^{-1}) is the effective extinction coefficient, combining intrinsic absorption and scattering losses from powder particles. The incident laser intensity I_0 has a Gaussian distribution along the beam radius and results in the highest heat flux at the center of the irradiation spot. This absorbed energy initiates a multiphysical thermal cycle. The solid powder particles undergo a phase transformation, forming a melt pool. This liquid phase then coalesces and solidifies, creating a strong metallurgical bond between adjacent scan tracks and successive layers [24]. In order to accurately simulate this entire process, a comprehensive energy balance and multi-physics are necessary. Alongside the energy absorption anticipated by the Beer-Lambert law, it is necessary to consider losses through conduction to the surrounding particles and substrate, convection from the surface to the inert process gas, and radiation. Additionally, the latent heat dissipated during the phase change needs to be included in the thermal-numerical model [25].

Multidisciplinary SLS simulations are computationally complex and time-consuming due to the interaction of several physical phenomena. For efficient numerical modelling, the following simplifications have been implemented:

(1) The powder bed is modeled as a continuous, homogeneous medium consisting of uniformly sized, tightly packed, idealized spherical particles. This approximation eliminates particle-scale scattering effects while sufficiently capturing bulk thermal behavior for melt pool evolution.
(2) A Gaussian heat source is employed, neglecting angle-dependent absorption and powder-shading effects. These mechanisms contribute minor corrections in polymer SLS due to lower reflectivity and smaller optical path variations, and their omission enables a significant reduction in computational cost.
(3) Vaporization and recoil pressure are not considered. Unlike metal PBF, polymer SLS operates far below vaporization thresholds; therefore, recoil-driven flow instabilities, spatter, or keyhole formation do not occur and can be safely neglected.
(4) A two-dimensional (2D) model is used to analyze the dominant thermodynamic and melting dynamics. The 2D approach is well aligned with the objective of resolving vertical heat transfer and melt pool penetration efficiently, enabling transient multiphysics coupling without the high computational expense of a full 3D domain.
(5) Surface-tension-driven phenomena such as Marangoni convection and crystallization kinetics are excluded. In polymers, surface tension gradients are significantly weaker than in metals, and their contribution to melt pool circulation is limited. Similarly, crystallization kinetics mainly influence post-solidification microstructure rather than the transient melt pool geometry. Their omission allows computational efficiency while preserving accurate prediction of global thermal gradients, melt pool shape, and parameter-dependent trends.

2.2 Governing equations

2.2.1 Heat transfer

The SLS method is essentially a thermal manufacturing process. In this method, energy is transferred from the laser power source to the powder surface. This transmission is calculated using the generalized 2D heat transfer equation (Eq. 2) and is directly related to the standard energy conservation model [26].

$$d_z \rho\, c_p \frac{\partial T}{\partial t} + d_z \rho\, c_p u.\nabla T = \nabla \bullet (k \nabla \mathrm{T}) + d_z Q \tag{2}$$

Where $d_z$represents the effective layer thickness used to convert volumetric heat terms into an equivalent two-dimensional formulation, $\rho\, c_p \frac{\partial T}{\partial t}$ denotes the transient thermal storage, and $\rho\, c_p \mathrm{u} \cdot \nabla T$ describes the convective transport of energy within regions where molten PEEK exhibits flow. The term $\nabla \cdot (k \nabla T)$ accounts for in-plane heat conduction in the powder bed and melt pool, while Q represents the volumetric heat source associated primarily with laser absorption. In the context of SLS, the dominant source is the laser energy absorption ($d_z Q$), often modeled as a Gaussian heat source moving along the scan path. Viscous dissipation and pressure terms are usually negligible for polymers at the scales of SLS.

Initially, the ambient temperature and powder temperature (T_0) are assumed to be preheated to 583 K.

$$T(x,\, y, z)_{t=0} = T_0 \tag{3}$$

Apart from the upper surface, it is presumed that every other edge of the substrate is insulated. Thus, Eq. 4 defines the heat flux boundary condition to be performed to the surfaces of the solution domain.

$$-k\left(\frac{\partial T}{\partial z}\right)_{z=0} = \alpha_A q(r) - h(T - T_0) - \sigma \epsilon (T^4 - T_0^4) \tag{4}$$

In this context, *q(r)* represents the heat flux at a distance *r* from the laser center (W/m^{-2}), *k* denotes the thermal conductivity ($W/m{\cdot}K$), σ signifies the Stefan–Boltzmann constant ($5.67 \times 10^{-8}\ W{\cdot}m^{-2}{\cdot}K^{-4}$), T_0 refers to the preheat temperature (K), and h shows the heat transfer coefficient ($W/m^{-2}{\cdot}K$).

Additionally, αA and ε denote the absorption coefficient and emissivity, respectively.

These equations (Eqs. 2, 3 and 4) comprehensively represent the transient thermal behaviour during laser irradiation. While accounting for conduction in the powder bed and convection in the molten regions, latent heat effects during phase change (discussed in the next section) are incorporated by modifying the effective heat capacity or adding phase-field coupling.

2.2.2 Melting and solidification

The phase field method was implemented to simulate the melting and resolidification behavior of PEEK powder. The method provides a representation of complex interface geometries within the melt pool. A continuous order parameter ϕ is introduced in Eq. 5 to distinguish between solid and liquid phases. Here $\phi = 0$ represents the solid state, $\phi = 1$ represents the liquid state, and intermediate values represent the dispersed interface region.

$$\frac{\partial \varphi}{\partial t} + u.\nabla \varphi = \nabla . \left(\frac{\gamma \lambda}{\epsilon_{pf}^2} \nabla \psi \right) \tag{5}$$

where u is the velocity field, ε_{pf} is the interface thickness parameter, γ is a coupling constant, and λ relates to interfacial energy. The auxiliary variable ψ denotes the chemical potential, defined as

$$\psi = -\nabla .(\epsilon_{pf}^2 \nabla \varphi) + (\varphi^2 - 1)\varphi + \frac{\epsilon_{pf}^2}{\lambda} \frac{\partial f}{\partial \varphi} \tag{6}$$

where $f(\phi)$ represents the free energy density functional of the system. The model parameters are related by

$$\lambda = \frac{3\epsilon_{pf}\sigma}{\sqrt{8}}, \quad \gamma = \chi \epsilon_{pf}^2 \tag{7}$$

where σ is the interfacial energy and χ a scaling factor. The interface thickness ε_{pf}, interface energy σ, and other constant material parameters in the model relate the diffuse interface to physical surface energy and mobility.

In order to additionally capture the latent heat effects during melting and solidification, the enthalpy-based method was also implemented. In this approach, the energy conservation equation is expressed as a function of enthalpy H (J/m^3), which incorporates both sensible and latent heat contributions (Eq. 8). The density and specific heat are defined as weighted averages of the solid and liquid phases, while the latent heat of fusion is introduced through an apparent heat capacity term within a small transition interval. This creates a "mushy zone" in which solid and liquid coexist, and material properties are smoothly blended according to the local phase fraction. In the present model, this phase fraction is represented by the phase-field variable ϕ, which varies smoothly from 0 (solid) to 1 (liquid). The enthalpy formulation and the phase-field method are thus thermodynamically coupled. H(T, ϕ) includes both sensible heat and the latent heat contribution $L\phi$, allowing the heat-transfer equation to account for energy absorbed or released during phase change, while the phase-field equation uses the same ϕ to track the progression of melting and solidification. This ensures a consistent linkage between the temperature field, enthalpy evolution, and interfacial dynamics without explicitly tracking the solid–liquid boundary. By doing so, the release and absorption of latent heat are consistently accounted for in the temperature–enthalpy relationship without explicitly tracking the interface [27].

$$H = \int_{T_{ref}}^{T} \rho C_p T$$

$$\rho = \theta_1 \rho_1 + \theta_2 \rho_2 \qquad \theta_1 + \theta_2 = 1$$

$$C_p = \frac{1}{\rho}(\theta_1 \rho_1 C_{p1} + \theta_2 \rho_2 C_{p2}) + L_{1\to 2}\frac{\partial \alpha_m}{\partial T} \qquad \alpha_m = \frac{1}{2}\frac{\theta_2 \rho_2 - \theta_1 \rho_1}{\theta_1 \rho_1 + \theta_2 \rho_2}$$

Where Cp, ρ, and $L_{(1\to 2)}$ represent the specific heat ($J/(kg{\cdot}K)$), density (kg/m^3) and latent heat from phase 1 to phase 2 (kJ/kg), respectively. In the phase transition, a mushy zone exists, characterised by heterogeneous material characteristics during the transition interval (ΔT_{1_2}).

2.2.3 Fluid flow

The fluid dynamics of molten PEEK in SLS are governed by the incompressible Navier-Stokes equations (Eq. 9). The system is constrained by the continuity equation (Eq. 10), which ensures mass conservation for an incompressible fluid.

$$\rho \frac{\partial u}{\partial t} + \rho (u \bullet \nabla) u = \nabla . (pI + K) + F_\sigma + (\rho - \rho_{ref}) g \tag{9}$$

$$(\nabla \bullet u) = 0 \tag{10}$$

where u represents the velocity vector, ρ denotes the density, p signifies the pressure, I is the identity tensor, and $K=\mu(\nabla u+(\nabla u)T$ indicates the viscous stress tensor with μ as the dynamic viscosity. The expression $(\rho-\rho ref)g$ denotes the buoyancy force according to the Boussinesq approximation.

A two-phase mixture formulation (Eq. 11) was used to represent both solid and liquid phases in a single domain.

The effective density and viscosity are expressed as weighted averages of the solid and liquid phases according to their volume fractions:

$$\rho = \rho_1 V_{f,1} + \rho_2 V_{f,2}, \quad \mu = \mu_1 V_{f,1} + \mu_2 V_{f,2} \tag{11}$$

with phase volume fractions defined as:

$$V_{f,1} = \frac{1-\varphi}{2}, \quad V_{f,2} = \frac{1-\varphi}{2}, \quad V_{f,1} + V_{f,2} = 1 \tag{12}$$

Here, ϕ is the phase-field order parameter introduced in previous section. This expression allows the fluid flow model to be directly coupled to the melting and solidification dynamics. As ϕ evolves, the local mixing properties provide a smooth transition between the solid and molten PEEK properties.

This fluid flow formulation provides a coherent representation of molten polymer dynamics in the powder bed by encompassing the redistribution of liquid PEEK and the stabilisation of solid-like areas. The model considers the velocity and pressure fields that govern melt pool stability, porosity removal, and densification, while ignoring secondary effects such as ambient gas flow, evaporation, or recoil pressure. Mechanisms driven by surface tension, such as Marangoni convection, are simplified by assuming the surface tension coefficient (F_σ) remains constant.

2.3 Gaussian heat source

A Gaussian heat source distribution was used to model the laser-powder interaction in the two-dimensional simulation domain. The Gaussian function (Eq. 13) allows the energy intensity to gradually decrease from the beam center to the edges (along the x-axis). The decrease in energy penetration through the powder layer due to scattering and partial absorption within the porous medium in the vertical z-axis is depicted by a Beer-Lambert function (Eq. 1).

$$Q(x,z) = \frac{2\alpha_A P}{\pi {w_0}^2} exp\left[-2\frac{\left[x-(x_0+v_b \bullet t)^2\right]}{{w_0}^2}\right] exp\left[-\frac{|z|}{\Delta}\right] \tag{13}$$

where P is the laser power (W), α_A is the absorptivity of PEEK powder, w_0 is the laser beam radius (m), v_b is the scan speed (m/s), and Δ denotes the penetration depth, approximated by the effective layer thickness. The absorptivity value ($\alpha A = 0.63$) was selected based on experimentally reported CO_2-laser absorption measurements for semi-crystalline PEEK powders, where surface roughness and particle-scale scattering increase effective absorption compared with bulk PEEK [18, 28]. The extinction coefficient β used in the Beer–Lambert attenuation term similarly follows values adopted in polymer SLS heat-transfer models, representing combined intrinsic infrared absorption and multi-scattering within the porous powder bed. It should be noted that using a constant absorptivity introduces a degree of uncertainty because PEEK's optical properties are temperature dependent. However, due to the scarcity of reliable temperature-dependent data, a representative mean value is commonly used in preliminary thermal modelling studies. This formulation allows the laser irradiance to be expressed as a surface-subsurface energy distribution rather than a fully volumetric source. Thereby, it reduces computational complexity while preserving the fundamental physical properties of energy deposition. The 2D model provides an effective and realistic description of the effects of the laser heat source on temperature gradients, melt pool evolution, and layer bonding during the SLS process.

2.4 Material thermophysical properties

This study utilised polyetheretherketone (PEEK) as the build material. PEEK is especially appealing for SLS-produced aerospace and biomedical components due to its semicrystalline structure, its ability to withstand elevated temperatures, and its strong mechanical performance [29]. Thermogravimetric analyses show that PEEK maintains its integrity up to approximately 550 °C, with the first degradation onset occurring around 575–580 °C [30]. This degradation primarily involves random chain scission of ether and ketone linkages, followed by thermo-oxidative reactions that progressively reduce molecular weight and lead to char formation.

During SLS processing, the powder undergoes repeated cycles of heating, melting, and solidification, requiring accurate characterization of its temperature-dependent thermophysical properties. The temperature-dependent properties of PEEK used in the analysis were obtained using analytical functions or interpolation tables derived from experimental measurements [31–33] and are summarized in Table 1. Argon gas, which is frequently employed as an inert atmosphere in SLS to reduce oxidation and thermal degradation of polymer particles, was filled into the computational domain outside the powder bed. The thermophysical properties of argon were obtained directly from the COMSOL materials library. Intermediate values were computed through piecewise cubic interpolation.

2.5 Numerical model and boundary conditions

A two-dimensional finite element model was used in COMSOL Multiphysics to study the thermophysical response of PEEK powder during SLS processing. The presented

Table 1 Temperature-dependent physical properties of PEEK [31–35]

PEEK properties	Symbol	Temperature/Value		Units
Density	$\rho(T)$	T ≤ 300 K	1300	$kg \cdot m^{-3}$
		300 < T ≤ 400	1300 − 0.2·(T − 300)	
		400 < T ≤ 616	1280 − 0.37·(T − 400)	
		616 < T ≤ 700	1200 − 0.95·(T − 616)	
		T > 700 K	1120	
Specific heat capacity	Cp	T ≤ 300 K	1100	$J \cdot kg^{-1} \cdot K^{-1}$
		300 < T ≤ 400	1100 + 3.5·(T − 300)	
		400 < T ≤ 500	1450 + 4.8·(T − 400)	
		500 < T ≤ 600	1930 + 1.7·(T − 500)	
		600 < T ≤ 620	2100 + 5·(T − 600)	
		620 < T ≤ 680	2200 + 0.66 ·(T − 620)	
		T > 680 K	2240	
Thermal conductivity	k	T ≤ 300 K	0.25	$W \cdot m^{-1} \cdot K^{-1}$
		300 < T ≤ 400	0.26	
		400 < T ≤ 573	0.27	
		573 < T ≤ 616	0.29	
		T > 616 K	0.32	
Dynamic viscosity	μ	T < 616 K	(solid; very large μ),	Pa.s
		616 ≤ T ≤ 673	1000+(− 21.6)·(T − 643)	
		673 < T ≤ 723	350+(− 5.5)·(T − 673)	
		723 < T ≤ 773	75+(− 1.3)·(T − 723)	
		T > 773 K	10	
Melting temperature	Tm	616		K
Melting Enthalpy	H	130		$J \cdot g^{-1}$
Thermal expansion	β	50		$x10^{-6} K^{-1}$

model is designed to capture the fundamental physics of laser-material interactions in a computationally efficient manner while preserving the multiphysics effects necessary to reproduce realistic thermal and phase change behavior. To simulate the scanning laser, a moving Gaussian heat flux was applied to the top surface using the Heat Transfer module to transfer heat from the powder bed. The phase transition of PEEK from solid to liquid and vice versa was incorporated using an enthalpy-based formulation (Eq. 8) that also considers latent heat. The Laminar Flow module has been incorporated into the model to determine the polymer flow in the molten region. Additionally, the Non-Isothermal Flow module incorporated into the model provided a consistent coupling between the two domains, ensuring an accurate representation of convective transport and viscosity reduction at higher temperatures. Surface tension effects were also considered to simulate neck formation between neighboring powder particles. The lateral surfaces were assumed adiabatic to minimize artificial heat exchange, while the bottom boundary was constrained to reflect the conductive heat loss into the solid substrate. Convective and radiative heat dissipation at the top free surface was also included to approximate realistic energy losses to the surrounding argon atmosphere.

The schematic representation of the finite element domain and its dimensions is given in Fig. 2. A dense PEEK layer was defined as the solid substrate in the model, and a layer of PEEK powder particles of uniform diameter was placed on it to form a powder bed. For numerical discretization, a structured triangular mesh was employed, resulting in approximately 15,500 elements across the 2D computational domain. To ensure that the simulations were carried out within a mesh-independent range, the minimum and maximum element sizes were refined between 0.25 μm and 1.75 μm, with a maximum element growth rate of 1.08 and a curvature factor of 0.25. Additionally, a concise mesh-sensitivity check was performed using coarse (≈9,800 elements), medium (≈15,500 elements), and fine (≈27,400 elements) meshes, showing variations of < 3% in melt pool depth, < 3% in Heat-Affected Zone (HAZ) thickness, and < 2% in peak temperature. These negligible differences confirmed that the selected mesh resolution provides numerically stable and mesh-independent results.

The transient laser scanning was simulated using a moving Gaussian heat source, with calculations performed at 500 incremental time steps and a relative tolerance of 5×10^{-3}. The total simulated interaction covered a duration of 0.29 milliseconds, sufficient to capture both the heating and cooling stages of the process. For numerical solving, a parallel sparse direct solver (PARDISO) was selected to handle the coupled thermal–fluid equations efficiently. Each single-track analysis required approximately 5–7 min of computation time on a computer equipped with an Intel Core i5-4200 H processor and 8 GB DDR4 memory.

2.6 Simulation design and parametric analysis

A simulation framework was established to systematically analyze the influence of key operating parameters on the thermal and physical response of PEEK powder during the SLS process. In this two-dimensional model, laser power (P) and scanning speed (v) were defined as the main variables, while hatch space (h) was held constant at 0.2. Together, these factors determine the Energy Density (ED) in Eq. 4, a widely used metric that quantifies the effective

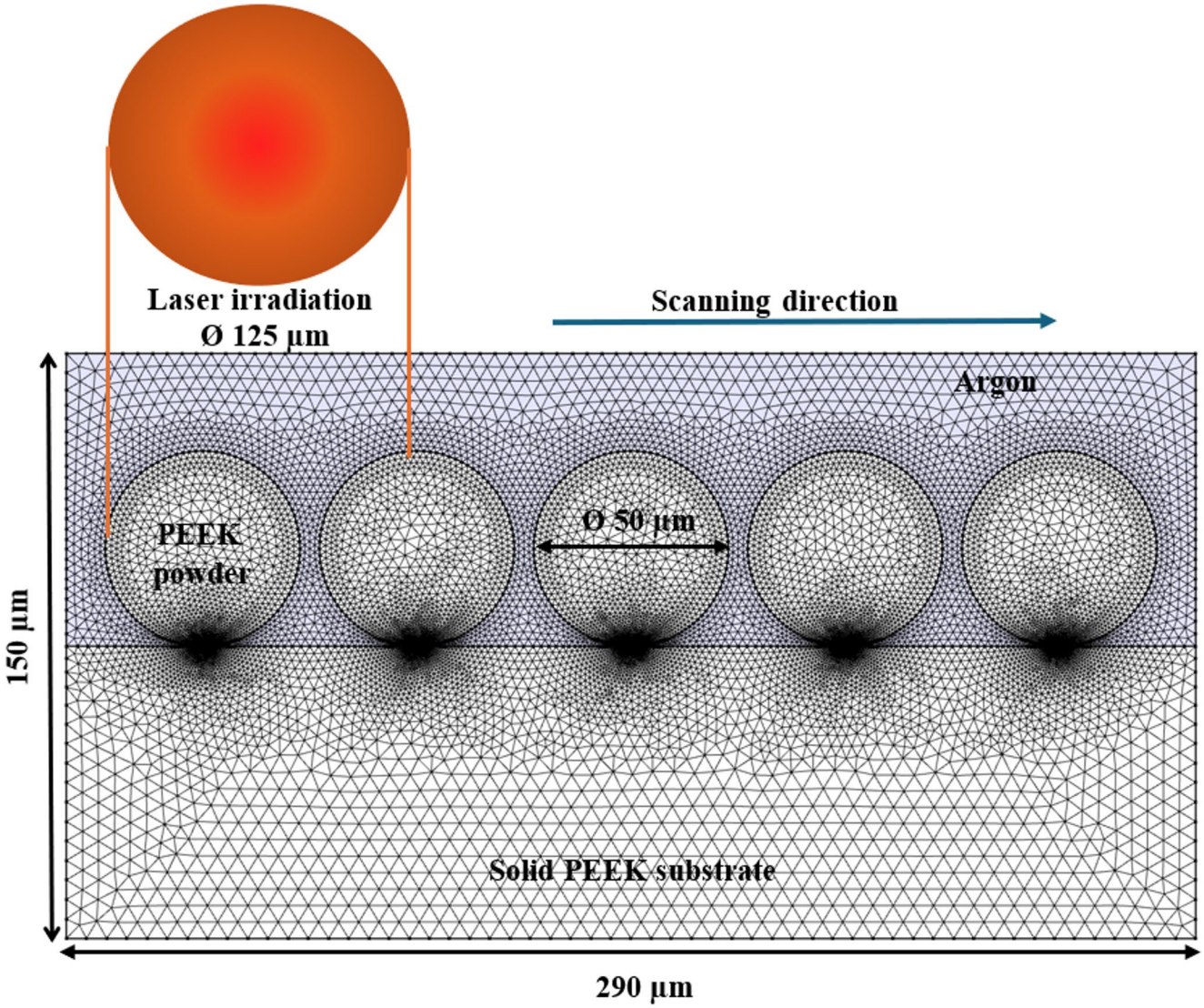


Fig. 2 Two-dimensional finite element model used to simulate the SLS process

energy delivered to the powder bed during laser exposure [36]. Previous research has demonstrated that energy density (ED) is a key factor in influencing part density, mechanical integrity, and surface quality [15, 23]. Insufficient ED often results in incomplete melting and lack-of-fusion defects, whereas excessively high values may cause material degradation, excessive shrinkage, or other thermal defects. This metric offers a useful method for comparing various parameter combinations; however, as the results will show, ED alone does not fully reflect the time-dependent effects of the laser-material interaction in SLS of PEEK.

$$ED = \frac{P}{v \bullet h} \tag{14}$$

The simulation design was structured into four categories based on increasing energy density (ED) values: low (0.015 J/mm²), moderate (0.03 J/mm²), upper-moderate (0.045 J/mm²), and high (0.06 J/mm²). To ensure consistency with experimental studies and established practice [37, 38], the scan speed was adjusted between 2000 and 4000 mm/s. Correspondingly, the laser power was varied from 6 W to 48 W in order to achieve the targeted ED levels. These parameter choices reflect typical settings of commercial SLS systems for PEEK, where powder sizes around 50 µm, 0.1 mm layer thickness, and scan speeds above 2000 mm/s are commonly used to prevent excessive heat accumulation. Slower scan speeds (< 1500 mm/s) were excluded because they promote overheating in high-temperature polymers and are impractical in commercial SLS systems due to substantially increased build times. The range selected in this study was therefore designed to capture the relevant process window and cover thermal gradients, melt pool evolution, and inter-particle neck growth. The eight parameter sets defined to represent this operating window are summarized in Table 2.

Table 2 Laser processing parameters in SLS

SET	Power (W)	Speed (mm/s)	ED (J/mm^2)	Constant Parameters [39]
1	6	2000	0.015	• Powder Bed Thickness: 0.1 [mm] • Spot Diameter: 0.25 [mm] • Powder Diameter: 50 [μm] • Hatch Space: 0.20 [mm] • Chamber Temperature: 583 [K] • Absorption coefficient: 0.63 • Argon atmosphere
2	12	2000	0.03	
3	18	2000	0.045	
4	24	2000	0.06	
5	12	4000	0.015	
6	24	4000	0.03	
7	36	4000	0.045	
8	48	4000	0.06	

3 Results and discussion

3.1 Transient temperature fields and thermal gradient evaluation

The time-dependent thermal distribution has been investigated to understand the interaction between laser energy input and material response during the SLS process. This enables the determination of optimal processing parameters by facilitating the detection of fusion defects caused by insufficient heating as well as thermal degradation caused by excessive heating. Figure 3 shows the simulated temperature evolution at the top and bottom surfaces of the powder layer for different laser parameter sets. In the figure, as the energy density (ED) increases, both the rate of temperature rise and the maximum surface temperatures increase proportionally. High energy input conditions (e.g., SET4 and SET8, both with ED = 0.06 J/mm²) caused the upper surface temperature to exceed PEEK's thermal degradation threshold (~ 833 K), leading to polymer degradation. These degradation limits (Tpd and Td), defined based on experimentally reported [23] onset temperatures for PEEK chain scission and thermo-oxidative reactions, help to distinguish a stable processing window from thermal conditions where significant molecular degradation is expected. Therefore, conditions exceeding Td are interpreted as falling outside the practical operating range even if complete melting occurs. Moreover, these excessive thermal exposures can negatively affect the strength and dimensional accuracy of the final part by causing keyhole-type porosity [40]. In contrast, low ED cases (e.g., SET1 and SET5, both with ED = 0.0015 J/mm²) produced maximum temperatures only slightly above the melting temperature of PEEK (~ 616 K). Furthermore, this temperature increase has been restricted to the upper surfaces of the powder. This inadequate heat transfer, which cannot penetrate the lower layers, limits the depth of the molten pool and reduces mechanical strength by causing defects such as weak interlayer bonding or incomplete melting [41]. Optimal thermal profiles were obtained in intermediate energy conditions (e.g., SET2 and SET6, both with ED = 0.03 J/mm²), where the temperature distribution remained within the desired processing window allowing for stable sintering without thermal damage. These results are consistent with previous numerical and experimental studies reporting similar trends in heat absorption and dissipation depending on energy density [15, 28, 39].

Figure 4 illustrates the peak surface temperatures (upper and lower) achieved across variations in laser power and

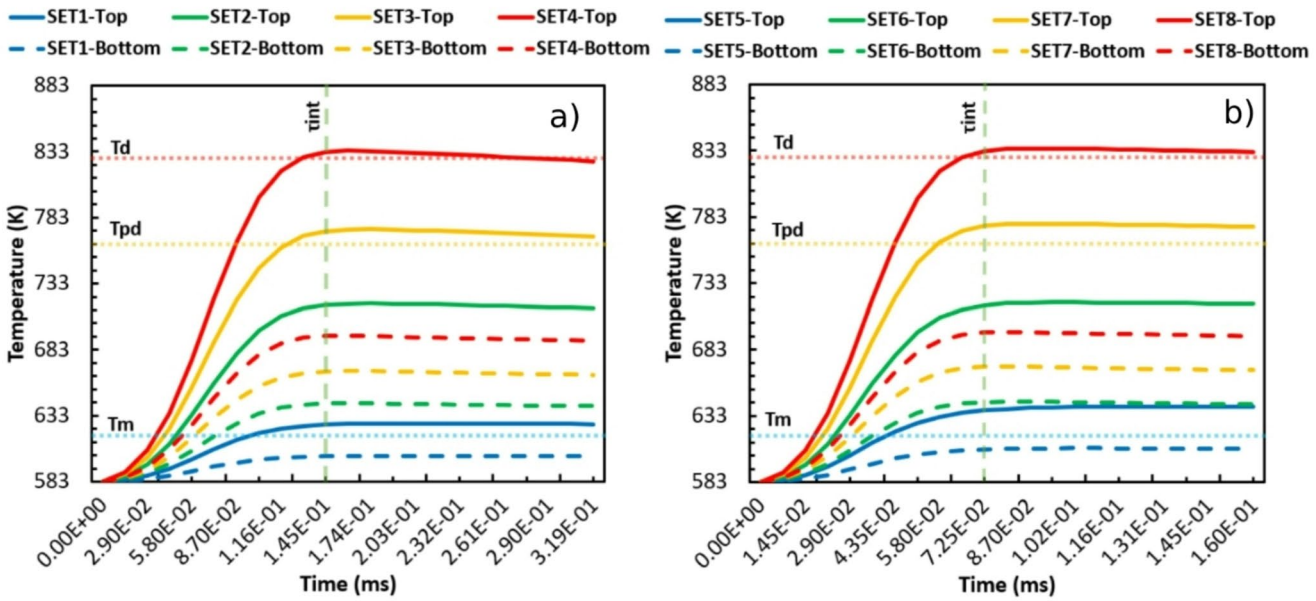


Fig. 3 Simulated temperature evolution at the top and bottom surfaces of the powder bed for different laser parameter sets. Horizontal lines mark Tm (melting), Tpd (partial degradation), and Td (full degradation); the vertical line indicates τint (interaction duration)

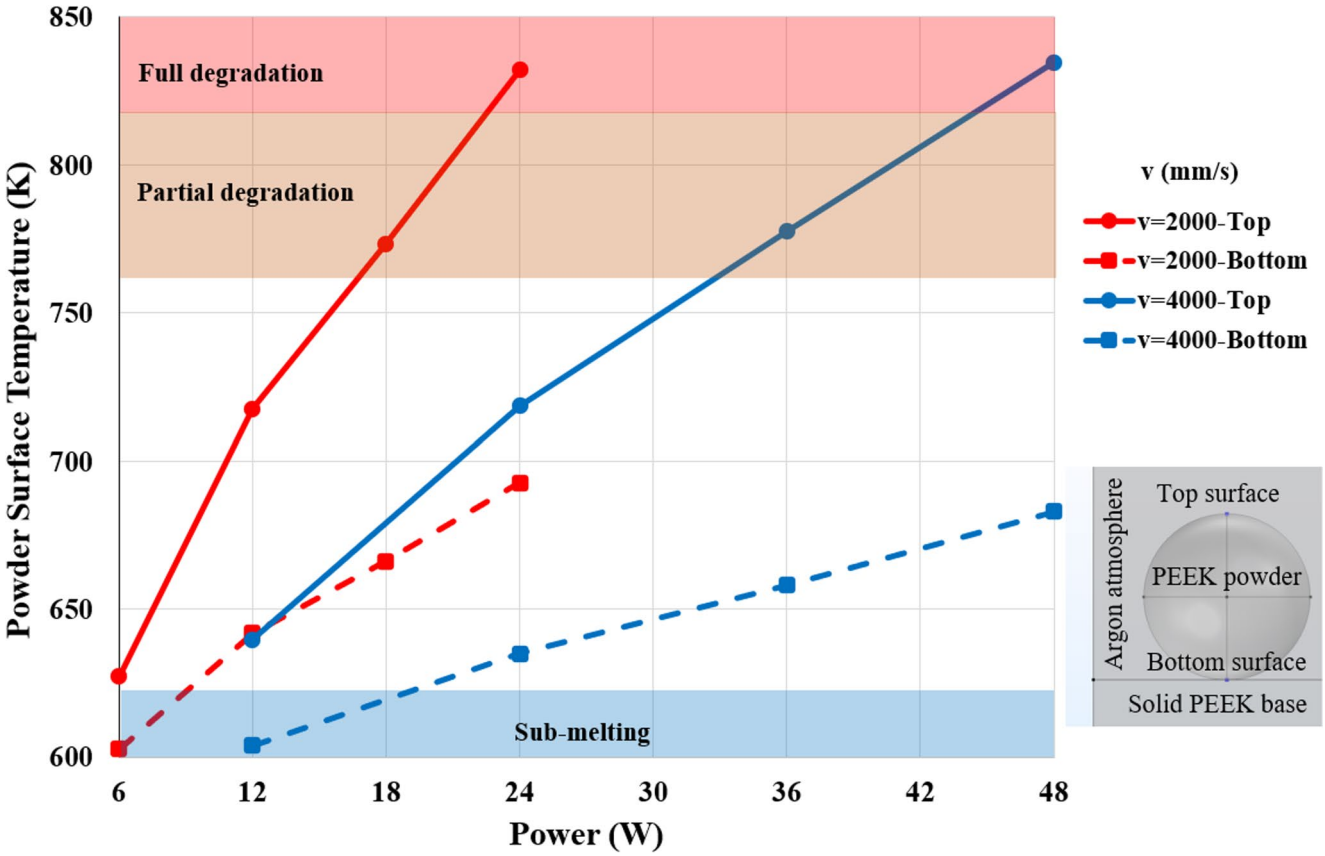


Fig. 4 Peak surface temperatures as a function of laser power at scan speeds of 2000 and 4000 mm/s

scanning speed. At low laser power levels (e.g., 6–12 W), the supplied energy is insufficient to achieve full melting, particularly in the bottom region of the powder bed. For instance, at 6 W the bottom surface remains close to 605–610 K, which is well below.

the melting temperature of PEEK (~616 K). Even at 12 W, the bottom surface only reaches ~635 K, still on the boundary of the sub-melting regime. This shows that especially at low powers, heat transfer into deeper layers is limited, and lowering the scan speed alone cannot compensate for the lack of input energy. As laser power increases, both top and bottom surface temperatures rise significantly. At 18 W, the bottom surface exceeds ~655 K, clearly above the melting range and enabling more effective sintering. At 24 W, bottom temperatures reach nearly 690 K, ensuring sufficient penetration, while the top surface climbs beyond 830 K, entering the full degradation regime. This indicates that, although higher powers are essential to prevent lack-of-fusion at the bottom surface, they also increase the risk of thermal degradation near the top surface, particularly at slower scanning speeds.

The temperature difference between the upper and lower surfaces increases as the energy density (ED) increases, as seen in Fig. 4. This can be explained by the non-linear heat transfer in the powder bed, as well as the more dominant local heating concentrated on the surface at high energy inputs. At higher ED levels, the upper surface temperature increases rapidly due to the laser beam transferring more energy in a short interaction time. However, due to the low thermal conductivity of PEEK powder (Table 1), especially when loosely packed, a substantial portion of this energy is trapped at the surface, and heat transfer to the lower layers remains limited. Furthermore, the increase in surface temperature at high ED values also increases radiative and convective heat losses from the upper layer, further restricting heat diffusion downward. This effect becomes more pronounced when the interaction time is insufficient to reach equilibrium.

Although scanning speed is included as a parameter in the energy density formulation (in Eq. 14), it should be considered separately since it directly governs the laser–material interaction time and thus the effective energy absorption. For a given ED, many different (P, v) pairs are possible. However, the local interaction time of the traveling beam with a point on the surface scales with $\tau_{int} \approx 2\ w_0/v$, and the characteristic thermal diffusion length in the powder bed scales with $L_d \sim \alpha\ \tau_{int}$. Consequently, cases with the same ED but different scan rates (e.g., SET1 and SET5) exhibit

different interaction times and diffusion lengths, which explains the difference in peak temperatures and melt pool depths despite having the same nominal energy input per unit area. As seen in Fig. 4, surface temperature rises nearly linearly with increasing laser power, yet the slope of this rise differs significantly with scan speed. At 2000 mm/s, the top surface enters the partial degradation regime at ~18 W and surpasses the full degradation threshold above 24 W, confirming that slower scanning promotes greater heat accumulation. Conversely, at 4000 mm/s, the temperature increase is more gradual, with partial degradation observed at higher powers (>36 W). Nevertheless, this decrease in interaction time at increased scanning speeds is offset by the limited thermal penetration, as evidenced by the increasing disparity between the top and bottom surface temperatures in Fig. 4. This temperature difference between the upper and lower surfaces indicates the presence of vertical thermal gradients in the melt pool. These gradients play an important role in determining the geometry of the melt pool and, if not properly controlled, can lead to permanent stresses and warping.

Figure 5 shows a comparative view of the transient thermal distributions in the powder bed according to laser parameters. The isothermal contours illustrate the evolution of thermal penetration, while the temperature scale bar below quantifies the thermal magnitude and defines the extent of the melting zone. The importance of interaction time is emphasised by a direct comparison between SET4 and SET6, which operate at varying scanning speeds but maintain the same 24 W laser power. In SET4, the reduced scanning speed facilitates extended energy deposition, leading to an expanded thermal zone with considerable vertical penetration into the substrate. Conversely, SET6, which processes twice as quickly (4000 mm/s), shows a flatter distribution with lower peak temperatures because the material receives less energy density. This reduced interaction time prevents overheating of the surface, but also limits subsurface heating. This results in a weaker thermal gradient and a risk of incomplete fusion in deeper layers. An analysis of SET6 and SET8, both operating at a scanning speed of 4000 mm/s, demonstrates the influence of laser power. The increased power utilised in SET8 doubles the energy density compared to SET6, resulting in a considerably more intense melt pool. However, the contours in the high-power SET8 reveal high peak surface temperatures (> 780 K) throughout the powder volume. This suggests a high risk of thermal degradation, in which PEEK powder undergoes chain scission and molecular weight reduction, leading to gas evolution, void formation, and carbonization [42].

The thermal results demonstrated that higher ED correlates with increased surface and subsurface temperatures, yet the inherently low thermal diffusivity of PEEK powder restricts downward heat flow, consequently magnifying the inter-surface temperature difference. Despite having identical ED values, altering the balance between laser power and scanning speed results in markedly different thermal profiles. This highlights the critical impact of the amount of energy transferred to the surface and the duration of interaction. Lower scanning speeds allowed for deeper heat penetration but increased the risk of surface degradation. Higher scanning speeds, on the other hand, resulted in more localized heating near the surface but inadequate melting in the subsurface region. These results emphasize the importance of considering both the magnitude of the energy input and the temporal dynamics of laser-material interaction to achieve stable melting and reliable interlayer bonding. To accurately capture these effects and their dependence on process parameters, a comprehensive study of the melt pool formation and morphology is therefore necessary.

3.2 Molten pool evolution

Figure 6 illustrates the transient evolution of the melt pool for various combinations of laser power and scan speed. Molten material is represented by red, while solid material is signified by blue. At low energy density (e.g., SET1 and SET5, ED = 0.015 J/mm²), the molten region remains shallow and discontinuous, with limited bonding between adjacent particles. In these cases, the bottom layers remain below the melting threshold, resulting in incomplete fusion and a high likelihood of lack-of-fusion defects. A comparison between SET1 and SET5 reveals more incomplete melting in SET1, which was processed with lower laser power (6 W). This clearly demonstrates that, despite having the same ED values, lower laser power is insufficient to provide adequate heat transfer into the powder bed. In the parameter sets with low laser power and high scanning speed (e.g., SET5, ED = 0.015 J/mm² and SET6, ED = 0.030 J/mm²), delays in neck formation are observed and the melted zone remains relatively shallow. Even in the last step of the scanning (at 0.29 ms), delays in the completion of the melted zone result in steep thermal gradients. Such delays and the shallow melt pool structure can lead to porosity, weak interlayer bonding, and finally reduced mechanical integrity of the final part. In SET3, characterized by a moderate ED and a slow interaction time, a homogeneous melt pool structure can be observed. This morphology indicates the feasibility of producing dense parts without allowing the formation of voids or lack-of-fusion defects. In SET4, however, the increased ED significantly enlarges both the melt pool and the Heat-Affected Zone (HAZ). Such a morphology can lead to problems such as excessive thermal stresses and distortion, ultimately resulting in dimensional inaccuracy and reduced part quality. Multi-physics-based animations of melting behaviour for varying ED levels are provided in Supplementary Materials 1.

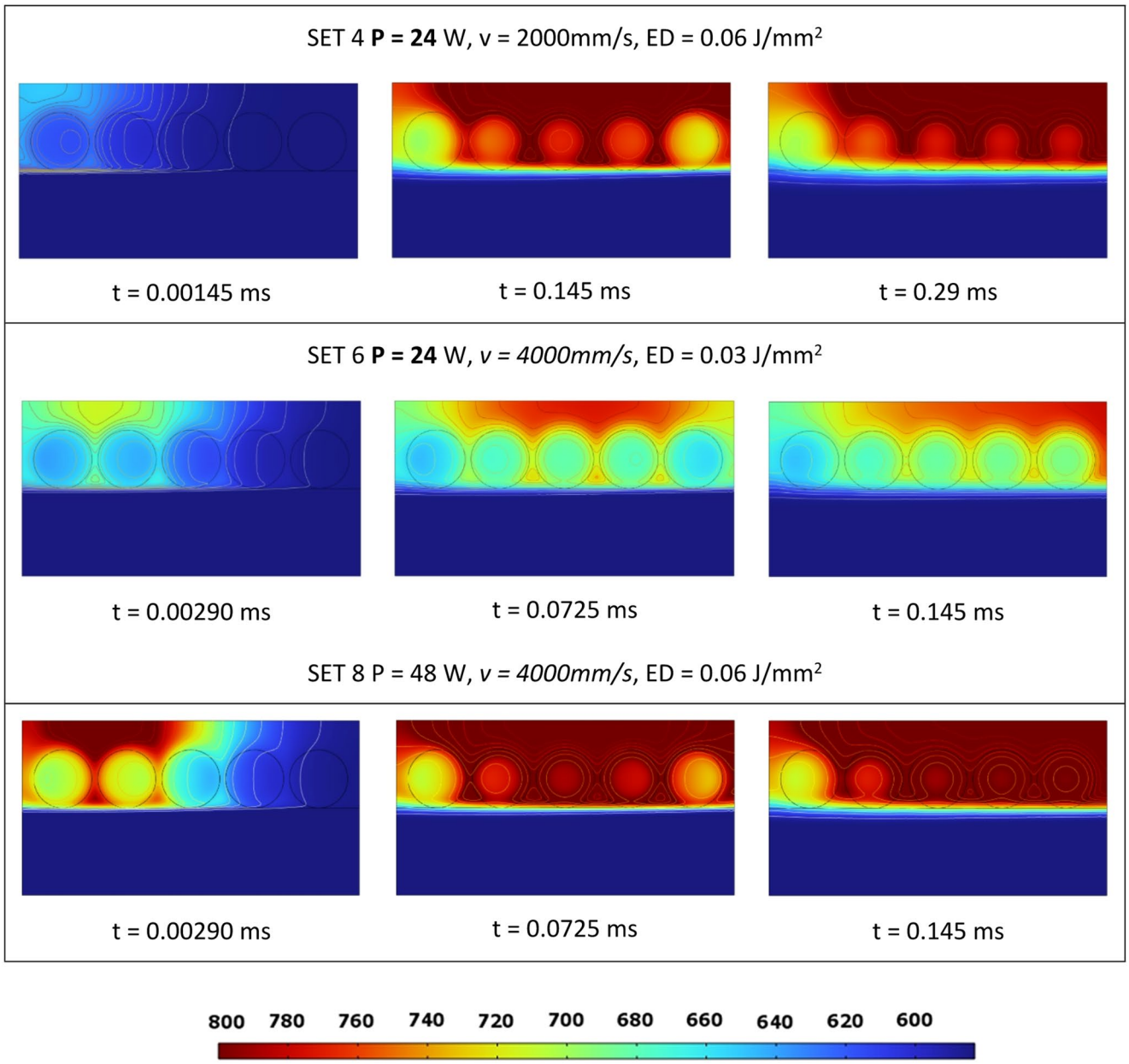


Fig. 5 Thermal distributions for SET4 (P = 24 W, v = 2000 mm/s), SET6 (P = 24 W, v = 4000 mm/s), and SET8 (P = 48 W, v = 4000 mm/s) at different time steps. Isothermal contours show heat penetration and melt pool evolution (600–800 K)

Figure 7 illustrates that the melt pool depth and HAZ size are distinctly governed by both the Energy Density (ED) and the transient dynamics of the laser-material interaction. At a constant scanning speed of 2000 mm/s (SET1–SET4), gradual increases in laser power from 6 W to 24 W widen the melt pool depth from ~56 µm to ~118 µm and the HAZ from ~67 µm to ~148 µm. This trend confirms the direct effect of increased power on the energy provided per unit area, thereby ensuring extensive phase transformation and profound heat transfer. At the higher scan speed of 4000 mm/s (SET5–SET8), a similar pattern is seen, with melt pool depths growing from ~61 µm to ~120 µm as power increases from 12 W to 48 W. Nevertheless, the incremental gains in melt penetration are slightly lower than those of the 2000 mm/s group due to the shorter interaction periods. It indicates that the thermal diffusion efficiency is significantly influenced by the exposure time. The inherently low thermal conductivity of PEEK (see Table 1) limits vertical heat transfer, meaning that insufficient interaction time, even at high laser powers, restricts subsurface fusion. At low power with a high scan rate (e.g., SET5), the melt pool remains relatively shallow, resulting in insufficient neck

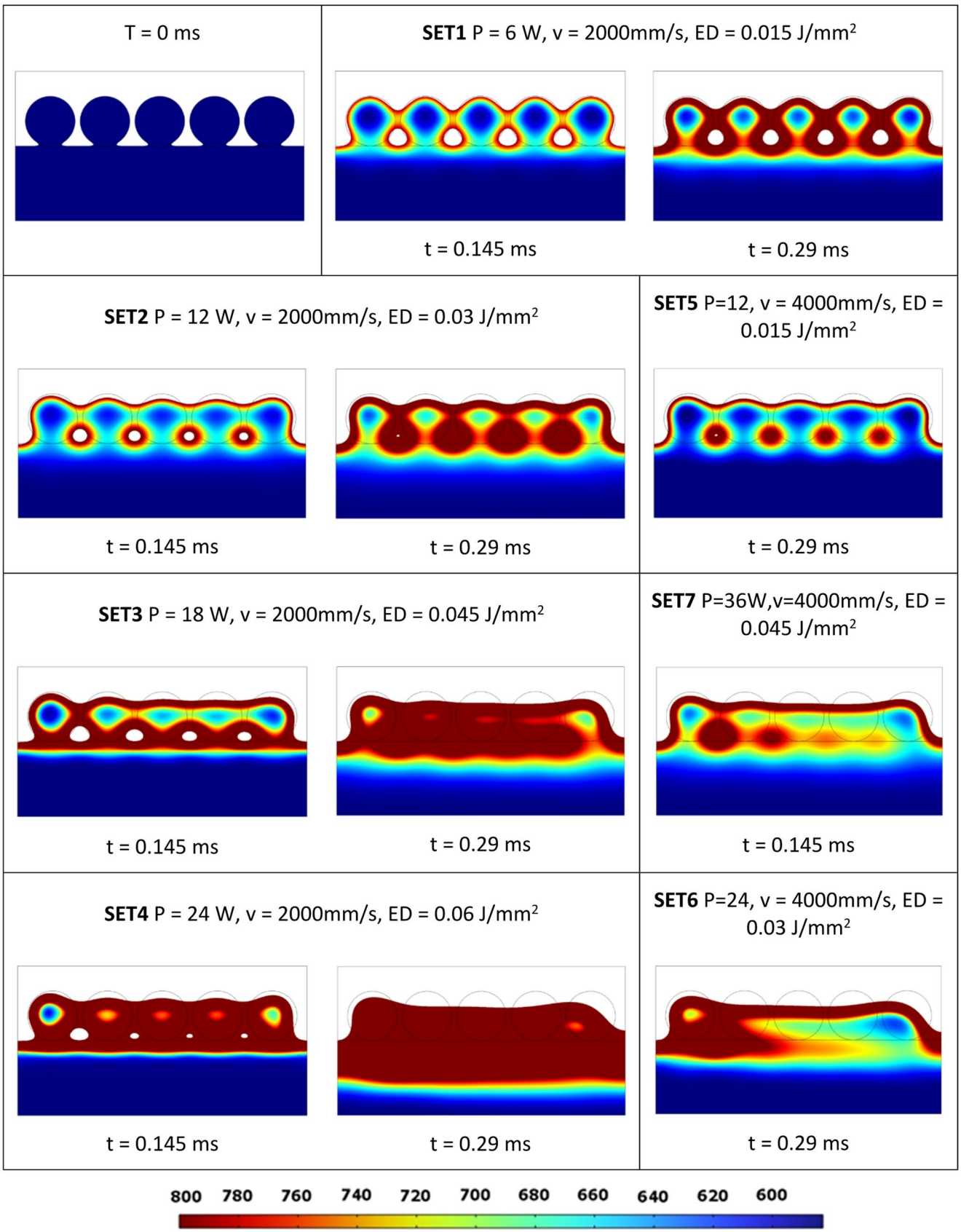


Fig. 6 Melt pool evolution for different parameter sets (SET1–SET7) at t = 0.145 ms and t = 0.29 ms, showing the effect of laser power, scan speed, and energy density (ED) on temperature distribution and melt pool morphology

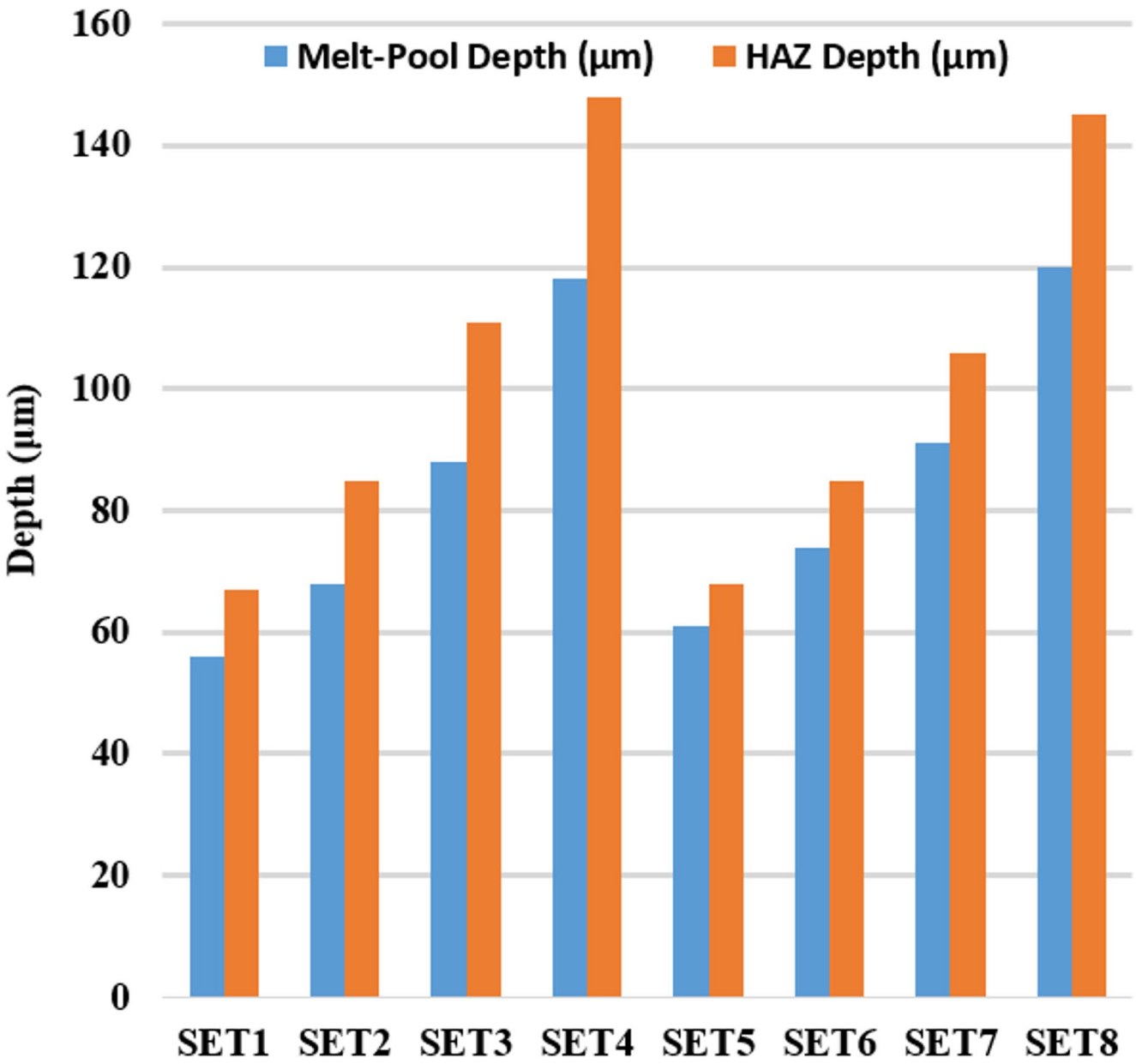


Fig. 7 Radar plot comparing melt pool depth (blue) and heat-affected zone (HAZ) depth (orange) for different parameter sets

growth and incomplete layer consolidation. In contrast, high-power conditions such as SET4 and SET8 create large HAZ regions and extensive melt pools. However, excessive heat input increases the risk of distortion, thermal stresses, and dimensional instability. Intermediate conditions (SET2, SET3, and SET6) exhibited a more stable melt pool behavior. These sets ensured proper sintering without surface overheating or uncontrolled HAZ growth.

Lastly, the simulated melt pool geometries show qualitative trends that are consistent with experimentally reported processing windows in the SLS of high-performance polymers such as PEEK. For instance, the predicted maximum surface temperature (≈ 370 °C) and melt pool depth (≈ 100 µm) are in close agreement with the experimental temperature ranges observed by Wang et al. [5] and Kigure et al. [17], thereby confirming that the use of sufficient energy density levels ensures interlayer diffusion without thermal degradation. The observed reduction in temperature gradient at moderate scanning rates is consistent with the results of Berretta et al. [16], who reported enhanced density and mechanical properties under similar laser conditions. Likewise, the simulated interlayer heat accumulation and subsequent cooling behavior are in line with the thermal field distributions modeled by Riedlbauer et al. [19] and experimentally verified by Peyre et al. [23], demonstrating that preheating near the crystallization temperature effectively

reduces residual stresses. The integration of an enthalpy-based phase change model and temperature-dependent thermal conductivity also reproduces the melt pool evolution trends reported by Mokrane et al. [18], validating the capability of the present framework to capture the coupled thermal and physical mechanisms of polymer sintering. The suggested approach demonstrates reliability as a predictive tool for evaluating process stability and determining appropriate operating windows in the SLS of high-performance polymers such as PEEK.

4 Conclusion

In this study, a two-dimensional multi-physics finite element model is presented to investigate the thermal and melt pool behavior of PEEK during SLS. The simulation results indicated that the energy density (ED) is a critical factor in determining the melt pool depth, heat-affected zone (HAZ) size, and temperature uniformity throughout the powder bed. Optimal thermal and morphological conditions were achieved at a moderate energy density (≈ 0.03 J/mm^2), facilitating melting and interlayer bonding while minimizing thermal deterioration. Insufficient energy density resulted in partial fusion and poor interlayer bonding, whereas excessive energy input caused overheating and possible polymer degradation.

The modeling framework developed in this study successfully coupled transient heat transfer, phase transformation, and fluid flow in a computationally efficient 2D domain. The model integrated an enthalpy-based phase change formulation with a Gaussian heat source and non-isothermal flow coupling, effectively capturing the evolution of the melt pool, interlayer temperature gradients, and the reduction of dynamic viscosity with high temporal precision. The results demonstrate that the proposed framework is a reliable tool for analyzing process parameters and predicting sintering quality in high-temperature polymer systems, thereby reducing the need for costly trial-and-error experiments. Overall, the findings establish a physically meaningful and computationally efficient basis for exploring laser–material interaction mechanisms in high-temperature polymer SLS. This work should therefore be viewed as a preliminary multiphysics analysis, intended to elucidate dominant thermal trends and support parameter selection prior to more resource-intensive 3D simulations.

Future research will focus on extending this two-dimensional model to a full three-dimensional transient analysis to capture lateral heat accumulation and the influence of scan path strategies. Incorporating crystallization kinetics and viscoelastic deformation into the model would enhance the prediction of residual stresses and shrinkage, thereby improving its capability to simulate mechanical behavior post-sintering. Machine learning-assisted surrogate modeling could also be integrated with the FEA results to accelerate parameter space exploration and further support predictive control in polymer SLS manufacturing.

Supplementary Information The online version contains supplementary material available at https://doi.org/10.1007/s00339-025-09288-y.

Acknowledgements This research did not receive any specific grant from funding agencies in the public, commercial, or not-for-profit sectors.

Author contributions O. E: Writing – original draf, investigation, methodology, investigation, conceptualization, supervision, methodology, formal analysis.

Funding Open access funding provided by the Scientific and Technological Research Council of Türkiye (TÜBİTAK).

Data availability The data that support the findings of this study are available from the corresponding author upon reasonable request.

Declarations

Conflict of interest The author declares that they have no known competing financial Interests or personal relationships that could have appeared to influence the work reported in this paper.

Open Access This article is licensed under a Creative Commons Attribution 4.0 International License, which permits use, sharing, adaptation, distribution and reproduction in any medium or format, as long as you give appropriate credit to the original author(s) and the source, provide a link to the Creative Commons licence, and indicate if changes were made. The images or other third party material in this article are included in the article's Creative Commons licence, unless indicated otherwise in a credit line to the material. If material is not included in the article's Creative Commons licence and your intended use is not permitted by statutory regulation or exceeds the permitted use, you will need to obtain permission directly from the copyright holder. To view a copy of this licence, visit http://creativecommons.org/licenses/by/4.0/.

References

1. Y. Liu, F. Zhao, Y. Zhao, T. Shu, S. Liu, S. Wang, Y. Su, C. Sun, S.N. Varma, C. Liu, Build orientation effects on properties of SLS-printed PEEK for bone implants: surface-physical-mechanical characteristics and in vitro cellular responses. J. Mater. Res. Technol. (2025). https://doi.org/10.1016/j.jmrt.2025.09.169
2. M.H. Ali, N. Sabyrov, E. Shehab, Powder bed fusion–laser melting (PBF–LM) process: latest review of materials, process parameter optimization, application, and up-to-date innovative technologies. Prog. Addit. Manuf. **7**(6), 1395–1422 (2022)
3. Y. Yamauchi, T. Kigure, T. Niino, Optimization of penetration depth and powder layer thickness for proper interlayer adhesion in polymer laser sintering. 2022
4. S. Singh, D. Kaur, M. Singh, R. Balu, A. Mehta, H. Vasudev, Challenges and issues in manufacturing of components using

polymer-based selective laser sintering (SLS): a review. Int. J. Interact. Des. Manuf. (IJIDeM) , 1–24 (2024)
5. Y. Wang, K. Chai, Y. Wang, Study on the temperature field distribution of the interface and process parameter optimization for selective laser sintering of PEEK. Polymer Engineering & Science **65**(6), 3302–3318 (2025). https://doi.org/10.1002/pen.27215
6. M.M. Rahman, K.A. Ahmed, M. Karim, J. Hassan, R. Roy, B. Bustami, S.M.N. Alam, H. Younes, Optimization of selective laser sintering three-dimensional printing of thermoplastic polyurethane elastomer: a statistical approach. J. Manuf. Mater. Process. **7**(4), 144 (2023)
7. A. Franco, M. Lanzetta, L. Romoli, Experimental analysis of selective laser sintering of polyamide powders: an energy perspective. J. Clean. Prod. **18**(16–17), 1722–1730 (2010)
8. H.M. Yehia, A. Hamada, T.A. Sebaey, W. Abd-Elaziem, Selective laser sintering of polymers: process parameters, machine learning approaches, and future directions. J. Manuf. Mater. Process. **8**(5), 197 (2024)
9. J. Borah, M. Chandrasekaran, Modeling and Optimization of 3D Printing Processes: A Literature Review. Rob. Autom. Healthc. , 95–114 (2024)
10. M. Schmid, R. Kleijnen, M. Vetterli, K. Wegener, Influence of the origin of polyamide 12 powder on the laser sintering process and laser sintered parts. Appl. Sci. **7**(5), 462 (2017)
11. M. Yuan, J.A. Galloway, R.J. Hoffman, S. Bhatt, Influence of molecular weight on rheological, thermal, and mechanical properties of PEEK. Polym. Eng. Sci. **51**(1), 94–102 (2011)
12. J. Molinar-Díaz, A.J. Parsons, I. Ahmed, N.A. Warrior, L.T. Harper, Poly-ether-ether-ketone (PEEK) biomaterials and composites: challenges, progress, and opportunities. Polym. Rev. **65**(2), 527–565 (2025)
13. N. Yi, R. Davies, A. Chaplin, P. McCutchion, O. Ghita, Slow and fast crystallising poly aryl ether ketones (PAEKs) in 3D printing: crystallisation kinetics, morphology, and mechanical properties. Additive Manuf. **39**, 101843 (2021)
14. A. Curmi, A. Rochman, J. Buhagiar, Influence of polyether ether ketone (PEEK) viscosity on interlayer shear strength in screw extrusion additive manufacturing. Additive Manuf. **84**, 104086 (2024)
15. M. Schmidt, D. Pohle, T. Rechtenwald, Selective Laser Sintering of PEEK. CIRP Annals **56**(1), 205–208 (2007). https://doi.org/10.1016/j.cirp.2007.05.097
16. S. Berretta, *Poly Ether Ether Ketone (PEEK) Polymers for High Temperature Laser Sintering (HT-LS)* (University of Exeter (United Kingdom), 2015)
17. T. Kigure, Y. Yamauchi, T. Niino, Investigation into laser sintering of PEEK using commercially available low powder bed temperature machine. 2021
18. A. Mokrane, Mh. Boutaous, S. Xin, Process of selective laser sintering of polymer powders: modeling, simulation, and validation. Comptes Rendus. Mécanique **346**(11), 1087–1103 (2018)
19. D. Riedlbauer, M. Drexler, D. Drummer, P. Steinmann, J. Mergheim, Modelling, simulation and experimental validation of heat transfer in selective laser melting of the polymeric material PA12. Comput. Mater. Sci. **93**, 239–248 (2014)
20. F. Shen, W. Zhu, K. Zhou, L.-L. Ke, Modeling the temperature, crystallization, and residual stress for selective laser sintering of polymeric powder. Acta Mech. **232**(9), 3635–3653 (2021)
21. Z. Zhang, Y. Huang, A.R. Kasinathan, S.I. Shahabad, U. Ali, Y. Mahmoodkhani, E. Toyserkani, 3-dimensional heat transfer modeling for laser powder-bed fusion additive manufacturing with volumetric heat sources based on varied thermal conductivity and absorptivity. Opt. Laser Technol. (2019). https://doi.org/10.1016/j.optlastec.2018.08.012
22. O. Eren, 3D multi-physics finite element simulation of the selective laser sintering process for polyamide 12: effects of laser parameters on melt pool formations and sintering quality. Macromol. Theory Simul. (2025). https://doi.org/10.1002/mats.202500094
23. P. Peyre, Y. Rouchausse, D. Defauchy, G. Régnier, Experimental and numerical analysis of the selective laser sintering (SLS) of PA12 and PEKK semi-crystalline polymers. J. Mater. Process. Technol., 2015;225326–225336
24. A. Gobal, B. Ravani, Physical modeling for selective laser sintering process. J. Comput. Inf. Sci. Eng. **17**(2), 021002 (2017)
25. E. Mirkoohi, D.E. Seivers, H. Garmestani, S.Y. Liang, Heat source modeling in selective laser melting. Materials. **12**(13), 2052 (2019)
26. J.C. Nelson, *Selective Laser Sintering: a Definition of the Process and an Empirical Sintering Model* (The University of Texas at Austin, 1993)
27. L. Xin, M. Boutaous, S. Xin, D.A. Siginer, Numerical modeling of the heating phase of the selective laser sintering process. Int. J. Therm. Sci. **120**, 50–62 (2017)
28. A. Korycki, C. Garnier, N. Rodier, F. Chabert, E. Laurent, and Nassiet V. Numerical and experimental analysis of the thermal profile of printed layers during selective laser sintering process of poly (etheretherketone). in *AIP Conference Proceedings*. 2019. AIP Publishing LLC
29. A. Haleem, M. Javaid, Polyether ether ketone (PEEK) and its manufacturing of customised 3D printed dentistry parts using additive manufacturing. Clin. Epidemiol. Global Health. **7**(4), 654–660 (2019)
30. P. Patel, T.R. Hull, R.E. Lyon, S.I. Stoliarov, R.N. Walters, S. Crowley, N. Safronava, Investigation of the thermal decomposition and flammability of PEEK and its carbon and glass-fibre composites. Polym. Degrad. Stab. **96**(1), 12–22 (2011)
31. R.D. Maksimov, J. Kubat, Time and temperature dependent deformation of poly (ether ether ketone)(PEEK). Mech. Compos. Mater. **33**(6), 517–525 (1997)
32. J.D.D. Melo, D.W. Radford, Time and temperature dependence of the viscoelastic properties of PEEK/IM7. J. Compos. Mater. **38**(20), 1815–1830 (2004)
33. M. Lei, C.M. Hamel, K. Chen, Z. Zhao, H. Lu, K. Yu, H.J. Qi, Thermomechanical behaviors of polyether ether ketone (PEEK) with stretch-induced anisotropy. J. Mech. Phys. Solids **148**, 104271 (2021)
34. Netzsch, *PEEK: Polyetheretherketone*. High-Temperature Resistant Thermoplastics 2025 [cited 2025; Available from: https://analyzing-testing.netzsch.com/en-US/polymers-netzsch-com/high-temperature-resistant-thermoplastics/peek-polyetheretherketone
35. Xometry, *PEEK (PolyEtherEtherKetone) Datasheet*. 2025 [cited 2025; Available from: https://xometry.eu/wp-content/uploads/2020/09/datasheet-PEEK.pdf
36. M. Madžarević, Đ Medarević, S. Pavlović, B. Ivković, J. Đuriš, S. Ibrić, Understanding the effect of energy density and formulation factors on the printability and characteristics of SLS Irbesartan tablets—application of the decision tree model. Pharmaceutics **13**(11), 1969 (2021)
37. T. Czelusniak, F.L. Amorim, Influence of energy density on polyamide 12 processed by SLS: from physical and mechanical properties to microstructural and crystallization evolution. Rapid Prototyp. J. **27**(6), 1189–1205 (2021)
38. A. Nazarov, I. Skornyakov, I. Shishkovsky, Design of the SLS-machine for PEEK. Nano Tech. Appl. **1**(1), 1–9 (2018)
39. F. Lupone, E. Padovano, F. Casamento, C. Badini, Process phenomena and material properties in selective laser sintering of polymers: a review. Materials **15**(1), 183 (2021)
40. J.-B. Forien, N.P. Calta, P.J. DePond, G.M. Guss, T.T. Roehling, M.J. Matthews, Detecting keyhole pore defects and monitoring

process signatures during laser powder bed fusion: a correlation between in situ pyrometry and ex situ X-ray radiography. Addit. Manuf. **35**, 101336 (2020)
41. C.-Y. Liaw, J.W. Tolbert, L.W. Chow, M. Guvendiren, Interlayer bonding strength of 3D printed PEEK specimens. Soft Matter. **17**(18), 4775–4789 (2021)
42. D.K. Patel, A.H. Sakhaei, M. Layani, B. Zhang, Q. Ge, S. Magdassi, Highly stretchable and UV curable elastomers for digital light processing based 3D printing. Adv. Mater. **29**(15), 1606000 (2017)

Publisher's note Springer Nature remains neutral with regard to jurisdictional claims in published maps and institutional affiliations.